nanomaterials

MDPI

Article

Tunable Fano Resonance and Enhanced Sensing in a Simple Au/TiO_2 Hybrid Metasurface

Zhihui He *, Weiwei Xue, Wei Cui, Chunjiang Li, Zhenxiong Li, Lihui Pu, Jiaojiao Feng, Xintao Xiao, Xuyang Wang and Gang Li

School of Physics and Electronic Information, Yan'an University, Yan'an 716000, China; xueww@yau.edu.cn (W.X.); wcui@yau.edu.cn (W.C.); licj@yau.edu.cn (C.L.); lizx@yau.edu.cn (Z.L.); pulh@yau.edu.cn (L.P.); fengjj@yau.edu.cn (J.F.); xiaoxt@yau.edu.cn (X.X.); wangxx@yau.edu.cn (X.W.); ligang0311@csrc.ac.cn (G.L.)

* Correspondence: hezh@yau.edu.cn; Tel./Fax: +86-091-1265-0504

Received: 25 February 2020; Accepted: 3 April 2020; Published: 5 April 2020

Abstract: We investigate Fano resonances and sensing enhancements in a simple Au/TiO_2 hybrid metasurface through the finite-different time-domain (FDTD) simulation and coupled mode theory (CMT) analysis. The results show that the Fano resonance in the proposed simple metasurface is caused by the destructive interaction between the surface plasmon polaritons (SPPs) and the local surface plasmon resonances (LSPRs), the quality factor and dephasing time for the Fano resonance can be effectively tuned by the thickness of Au and TiO_2 structures, the length of each unit in x and y directions, as well as the structural defect. In particular, single Fano resonance splits into multiple Fano resonances caused by a stub-shaped defect, and multiple Fano resonances can be tuned by the size and position of the stub-shaped defect. Moreover, we also find that the sensitivity in the Au/TiO_2 hybrid metasurface with the stub-shaped defect can reach up to 330 nm/RIU and 535 nm/RIU at the Fano resonance 1 and Fano resonance 2, which is more than three times as sensitive in the Au/TiO_2 hybrid metasurface without the stub-shaped defect, and also higher than that in the TiO_2 metasurface reported before. These results may provide further understanding of Fano resonances and guidance for designing ultra-high sensitive refractive index sensors.

Keywords: Fano resonance; plasmonics; sensors

1. Introduction

Surface plasmons (SPs) are collective oscillations of excited electrons at the interface between the metal and dielectric, which can effectively confine and enhance the electric filed [1–4]. Thus, SPs have important applications in the field of optical sensings, lasers, photovoltaics, and so on [5–9]. Local surface plasmon resonances (LSPRs) is one kind of SPs, which are strongly confined at the surface of metal nanostructures with non-ignorable losses [10–14]. Compared with LSPRs, Surface plasmon polaritons (SPPs) can propagate along the interface with lower losses [15–19]. Many interesting optical phenomena and applications based on LSPRs and SPPs are studied in a variety of nanostructures, such as Fano resonances and plasmon induced transparency (PIT) in nanoparticles or metal-dielectric-metal coupled waveguides [20–30], breaking the optical diffraction limit based on SPs [31,32], extraordinary optical transmission (EOT) in metallic nanohole [33–35], enhanced refractive index sensing and slow-light effects in metamaterials and coupled waveguide systems [36–45].

Fano resonances are caused by the destructive interference between the discrete and continuous states. Different from Lorentz lines, Fano resonances form asymmetric spectral lines, which have very high slope spectra and strong dispersion; the strongly confined electric fields can great enhance the interaction between the light and matters. Thus, Fano resonances are widely used to design ultra-high

sensitive sensors in variety of structural systems, such as metamaterials [46–49], metal-dielectric-metal waveguides [50,51], coupled graphene systems [52–54], and so on. Nordlander et al. reported Fano resonances in plasmonic nanostructures and metamaterials [46]. Singh et al. studied the ultra-sensitive terahertz sensing with high-Q Fano resonances in metamaterials [47]. Abujetas et al. investigated Fano resonances and the refractive index sensing in the all dielectric metasurface. They found that the ultra-narrow Fano resonances and the large figure of merit (FOM) due to the minimal loss of the silicon material [48]. Gerislioglu et al. discussed Fano resonances and sensing performances in the metallic metasurface [49]. Lu et al. discussed the plasmonic nanosensor based on Fano resonances in waveguide-coupled resonators [50]. Li et al. studied tunable nanoplasmonic sensors based on the asymmetric degree of Fano resonances in metal-dielectric-metal waveguides [51]. Tang et al. investigated sensing applications based on high-Q Fano resonances in graphene coupled systems [52]. Liu et al. reported high performance of refractive index sensing in the TiO_2 metasurface generated by the polarization insensitive Fano resonance [55]. Due to the strong optical fields binding characteristics of SPs, the metal and dielectric hybrid metasurface will enhance the sensitivity of the sensor based on Fano resonances. In addition, compared with the metallic metamaterials, narrow spectra of the Fano resonance can be realized in the metal and dielectric hybrid metamaterials. However, there are few studies about Fano resonances and its sensing enhancements in metal and dielectric hybrid metamaterials. Compared with metamaterials, metasurface is a new kind of two-dimensional artificial nanostructure, which is of low loss, easy fabrication, and has advantages in controlling light in nanoscale, so it has important applications in the field of integrated optical devices. Therefore, clarifying the generation and regulation mechanism of the Fano resonance in a simple and easy fabrication hybrid metasurface, and exploring sensing enhancements may play an important role in designing ultra-high sensitivity nano-sensors.

In this paper, we design an Au/TiO_2 hybrid metasurface and discuss Fano resonances and sensing enhancements in the proposed hybrid metasurface through the coupled mode theory (CMT) and finite-different time-domain (FDTD) simulation. The proposed hybrid metasurface structure is much simpler and easier fabrication than metamaterials. In addition, we find that Fano resonances can be effectively tuned by the structural parameters, the period, and the structural defect. In particular, the multiple Fano resonances can be observed in the Au/TiO_2 hybrid metasurface with the stub-shaped defect. At last, we investigate the sensing property in the proposed hybrid metasurface, and the result shows that the stub-shaped defect can effectively enhance the sensitivity in the Au/TiO_2 hybrid metasurface.

2. Structure and Theory Model

As shown in Figure 1a, we propose a metal and dielectric hybrid metasurface. The metal and dielectric are chosen to be Au and TiO_2, respectively, and the substrate is glass, the permittivity of Au, TiO_2, and glass reference to the related articles [35,55]. Figure 1b,c show the x–z plane view and x–y plane view of the proposed hybrid metasurface. l = 200 nm is the length of Au and TiO_2 structures, and h_1 and h_2 are the thickness of Au and TiO_2 structures, respectively. Px and Py are the length of each cell in the x- and y-directions, respectively. The transmission spectra of the proposed Au and TiO_2 hybrid metasurface are simulated by use of the FDTD simulation method. In this simulation, the effective area is divided into uniform Yee cells with the spatial step $\Delta x = \Delta y = \Delta z = 1$ nm and the time step $\Delta t = \Delta x/2c$ (c is the velocity of light in vacuum) [6], and the perfectly matched layer (PML) is chosen in the z-direction, and the periodic boundary condition is set in x- and y-directions [6,35]. The Gaussian beam with the x-directional polarization incidents from the positive direction of a z-axis in our simulation.

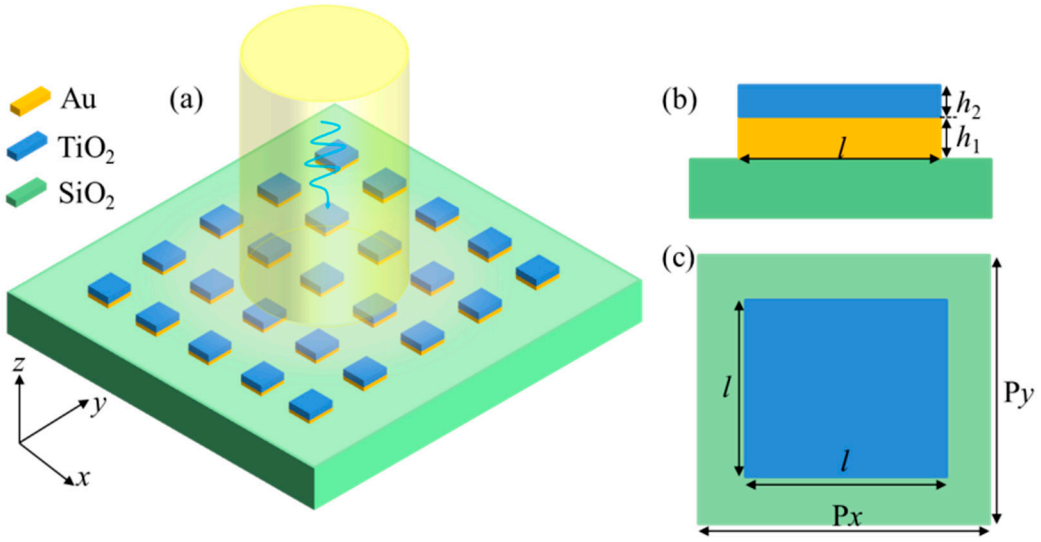

Figure 1. (**a**) schematic diagram of the Au/TiO_2 hybrid metasurface; (**b**) *x*–*z* plane view of the proposed hybrid metasurface; (**c**) *x*–*y* plane view of the proposed hybrid metasurface.

The transmission spectra of the proposed Au/TiO_2 hybrid metasurface are plotted in Figure 2. Figure 2a shows the transmission spectrum of the metasurface when there is only the Au structure on the substrate with h_1 = 90 nm, l = 200 nm, and Px = Py = 400 nm. We can see that a transmission dip appears at the wavelength of 705 nm. The inset of the Figure 2a depicts the electric field distribution Ez at the wavelength of 705 nm on the surface of the Au structure. We can see that the transmission dip is caused by the LSPRs at the boundary of the Au structure. Then, we investigate the transmission spectrum of the proposed Au/TiO_2 hybrid metasurface with h_1 = 90 nm, h_2 = 50 nm, l = 200 nm, and Px = Py = 400 nm. We can see that the typical Fano resonance spectrum can be observed in Figure 2b. The electric field distribution Ez on the interface between the Au and TiO_2 structure at the transmission peak and dips are shown in insets of Figure 2b. From the electric field distribution Ez, we can see that SPPs are excited at the interface between Au and TiO_2 structures, and the destructive interaction between the LSPRs and SPPs causes the Fano resonance in the proposed hybrid metasurface.

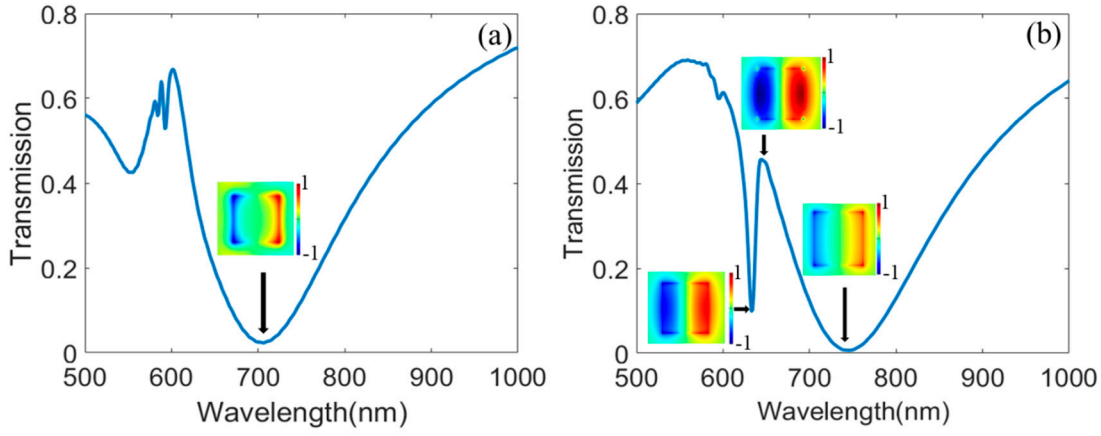

Figure 2. (**a**) transmission spectrum of the metasurface when there is only the Au structure on the substrate with h_1 = 90 nm, l = 200 nm, and Px = Py = 400 nm, the inset figure is the electric field distribution Ez at the wavelength of 705 nm, (**b**) transmission spectrum of the proposed Au/TiO_2 hybrid metasurface with h_1 = 90 nm, h_2 = *50* nm, l = 200 nm, and Px = Py = 400 nm, the insets are the electric field distributions Ez at the wavelength of 632.1 nm, 653.4 nm, and 737.6 nm.

In order to further understand Fano resonances in the proposed metasurface, we introduce CMT to theoretically analyze the generation and regulation mechanisms of Fano resonances. Based on coupling characteristics of resonant modes, we plot the schematic diagram of CMT for the proposed Au/TiO_2 hybrid metasurface as shown in Figure 3.

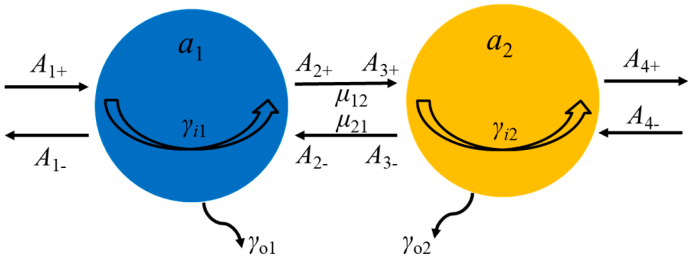

Figure 3. Schematic diagram of coupled mode theory (CMT) for the proposed Au/TiO_2 hybrid metasurface.

Here, a_1 and a_2 are defined as complex amplitudes of LSPRs and SPPs. ω is the angular frequency of the incident wave, and ω_1 and ω_2 are resonant angular frequencies of LSPRs and SPPs, respectively. $\gamma_{i1(2)} = \omega_{1(2)}/(2Q_{i1(2)})$ stands for the decay of LSPRs and SPPs due to the intrinsic loss, $Q_{i1(2)}$ are the quality factor of LSPRs and SPPs modes. $\gamma_{o1(2)} = \omega_{1(2)}/(2Q_{o1(2)})$ are the decays due to the energy escaping into the air, $Q_{o1(2)}$ are quality factors of coupling. $\mu_{12} = \mu_{21}$ is the direct coupling between LSPRs and SPPs in the proposed hybrid metasurface. $A_{N\pm}$ (N = 1, 2, 3, and 4) represent the amplitudes of the input and output waves. Thus, the CMT equation for our proposed hybrid metasurface can be expressed as follows [6,23]:

$$-\mathrm{j}\omega a_1 = (-\mathrm{j}\omega_1 - \gamma_{i1} - \gamma_{o1})a_1 + A_{1+}\sqrt{\gamma_{o1}} + A_{2-}\sqrt{\gamma_{o1}} + \mathrm{j}\mu_{12}a_2, \tag{1}$$

$$-\mathrm{j}\omega a_2 = (-\mathrm{j}\omega_2 - \gamma_{i2} - \gamma_{o2})a_2 + A_{3+}\sqrt{\gamma_{o2}} + A_{4-}\sqrt{\gamma_{o2}} + \mathrm{j}\mu_{21}a_1. \tag{2}$$

In order to solve the transmission coefficient of the proposed system, we assume ζ_1 and ζ_2 as:

$$\zeta_1 = \mathrm{j}\omega - \mathrm{j}\omega_1 - \gamma_{i1} - \gamma_{o1},\ \zeta_2 = \mathrm{j}\omega - \mathrm{j}\omega_2 - \gamma_{i2} - \gamma_{o2}. \tag{3}$$

Thus, Equations (1) and (2) can be simplified as:

$$\zeta_1 a_1 + A_{1+}\sqrt{\gamma_{o1}} + A_{2-}\sqrt{\gamma_{o1}} + \mathrm{j}\mu_{12}a_2 = 0, \tag{4}$$

$$\zeta_2 a_2 + A_{3+}\sqrt{\gamma_{o2}} + A_{4-}\sqrt{\gamma_{o2}} + \mathrm{j}\mu_{21}a_1 = 0. \tag{5}$$

Here, we assume that the light wave is lossless as it propagates through the space, so the law of energy conservation can be performed. Thus, the relationship among the $A_{N\pm}$ can be expressed as follows:

$$A_{2+} = A_{1+} - a_1\sqrt{\gamma_{o1}}, A_{4+} = A_{3+} - a_2\sqrt{\gamma_{o2}}, \tag{6}$$

$$A_{1-} = A_{2-} - a_1\sqrt{\gamma_{o1}}, A_{3-} = A_{4-} - a_2\sqrt{\gamma_{o2}}, \tag{7}$$

$$A_{3+} = A_{2+}\exp(\mathrm{j}\varphi), A_{3-} = A_{2-}\exp(-\mathrm{j}\varphi), \tag{8}$$

where φ is the indirect coupling phase between LSPRs and SPPs. In our proposed coupled mode system, we assume that A_4 equals to 0 in the proposed structure. Then, we apply Equations (6)–(8) to Equations (4) and (5). The transmission coefficient in the proposed hybrid metasurface $t = A_{4+}/A_{1+}$, Thus, the transmittance $T = |A_{4+}/A_{1+}|^2$ can be expressed as:

$$T = \left|\exp(\mathrm{j}\varphi) + \frac{\gamma_{i1}\zeta_2\exp(\mathrm{j}\varphi) + \gamma_{i2}\zeta_1\exp(\mathrm{j}\varphi) + \sqrt{\gamma_{i1}\gamma_{i2}}\exp(2\mathrm{j}\varphi)\chi_1 + \sqrt{\gamma_{i1}\gamma_{i2}}\chi_2}{\zeta_1\zeta_2 - \chi_1\chi_2}\right|^2, \tag{9}$$

with

$$\chi_1 = \sqrt{\gamma_{i1}\gamma_{i2}}\exp(j\varphi) + j\mu_{12},\ \chi_2 = \sqrt{\gamma_{i1}\gamma_{i2}}\exp(j\varphi) + j\mu_{21}. \quad (10)$$

3. Results and Discussion

3.1. Tunable Fano Resonances in the Hybrid Metasurface

Firstly, we investigate the dependence of Fano resonance on the thickness of the Au nanostructure h_1 in our proposed hybrid metasurface when h_2 = 50 nm, l = 200 nm, and Px = Py = 400 nm. Figure 4a shows transmission spectra as h_1 increases from 30 nm to 90 nm by use of the FDTD simulation method. The results show that there is no Fano resonance phenomenon when h_1 = 30 nm; this is because there is strong coupling between LSPRs and SPPs, the electric filed distribution Ez at the transmission dip as shown in the inset can explain this phenomenon as well. With the increasing of h_1, the direct coupling between LSPRs and SPPs decreases, and resonant wavelengths of LSPRs and SPPs show blue and red shift, respectively. Thus, the Fano resonance becomes more and more obvious as shown in Figure 4a. Then, we introduce the CMT to describe transmission spectra versus the thickness of the Au nanostructure as depicted in Figure 4b. From Figure 4a,b, we can see that FDTD simulation results are in agreement with CMT results.

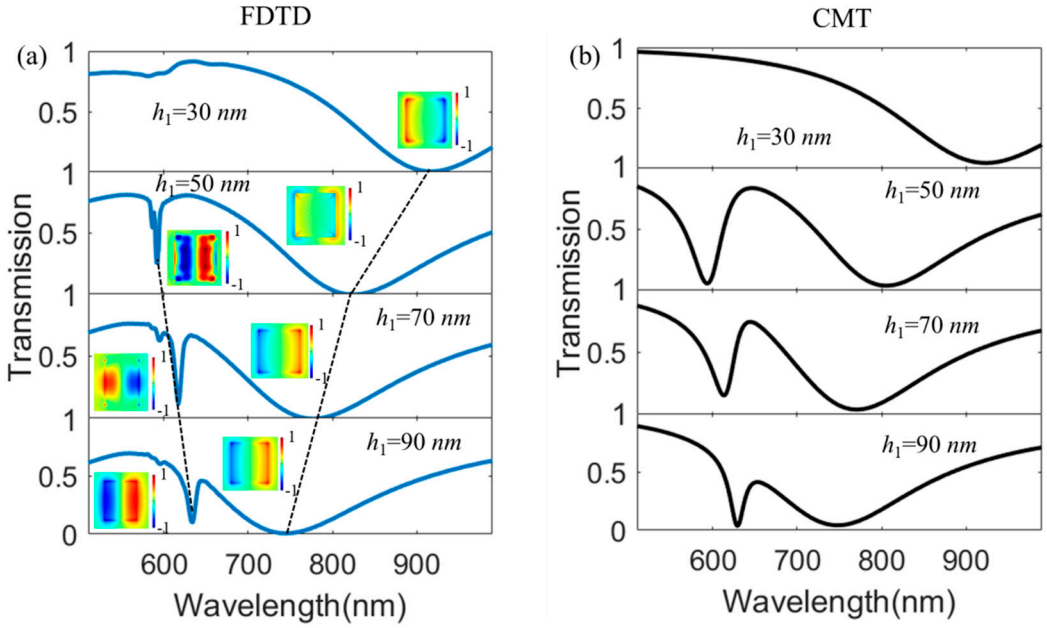

Figure 4. (**a**) FDTD simulation results of transmission spectra as a function of the thickness of h_1 for the proposed hybrid metasurface when h_2 = 50 nm, l = 200 nm, and Px = Py = 400 nm, the inset is the electric field distribution Ez at the transmission dips; (**b**) CMT results of transmission spectra as a function of the thickness of h_1 = 90 nm (φ = 0.48 π, Q_{i1} = 58, Q_{i2} = 406, Q_{o1} = 291, Q_{o2} = 300, and $\mu_{12} = \mu_{21} = 5.1 \times 10^{13}$), h_1 = 70 nm (φ = 0.48 π, Q_{i1} = 58, Q_{i2} = 387, Q_{o1} = 296, Q_{o2} = 305, and $\mu_{12} = \mu_{21} = 7.9 \times 10^{13}$), h_1 = 50 nm (φ = 0.48 π, Q_{i1} = 58, Q_{i2} = 356, Q_{o1} = 294, Q_{o2} = 301, and $\mu_{12} = \mu_{21} = 9.2 \times 10^{13}$), and h_1 = 30 nm (φ = 0.48 π, Q_{i1} = 58, Q_{i2} = 293, Q_{o1} = 289, Q_{o2} = 295, and $\mu_{12} = \mu_{21} = 15.4 \times 10^{13}$).

Then, we will discuss transmission spectra as a function of the thickness of TiO_2 layer as depicted in Figure 5. From Figure 5a, we can see that there are two transmission dips when h_2 = 30 nm. The left transmission dip is caused by SPPs on the interface between Au and TiO_2 layers, and the right transmission dip is the result of LSPRs. We can also see that the transmission ratio of the left transmission dip is very large as shown in Figure 5a because the thin TiO_2 layer can not effectively confine SPPs on the interface of Au and TiO_2 layers. As the thickness of TiO_2 layer h_2 increases, the transmission ratio of the left transmission dip decreases to zero as described in Figure 5b–d.

In particular, the Fano resonance becomes more and more obvious when h_2 increases from 30 nm to 90 nm.

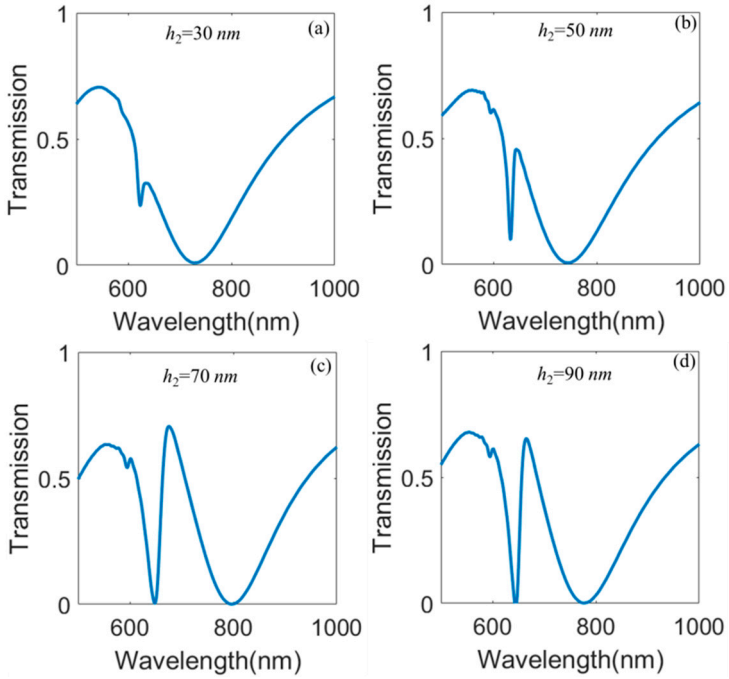

Figure 5. Transmission spectra as a function of the thickness of h_2 in the proposed hybrid metasurface when h_1 = 90 nm, l = 200 nm, and Px = Py = 400 nm.

Here, we introduce the definition of quality factor $Q_F = \delta/\omega_F - \omega_F/4\delta$ to discuss the Fano resonance in our proposed hybrid metasurface [56,57], where $\delta = |\omega_{D1} - \omega_{D2}|$, ω_{D1}, ω_{D2}, ω_F are resonant frequencies at the transmission dips and peak for the induced Fano resonance, respectively. In addition, the dephasing time of the Fano resonance is a critical parameter that can be defined by taking into account the resonant narrowness as follows [57]: $t_d = 2\hbar\delta$. The quality factor Q_F and dephasing time t_d of the Fano resonance in our proposed Au/TiO_2 hybrid metasurface as functions of the thichness h_1 and h_2 are shown in Table 1. From Table 1, we can see that the quality factor Q_F and dephasing time t_d increases when the thickness of the Au layer h_1 increases. For the factor h_2, we can see that the quality factor Q_F and dephasing time t_d do not change monotonically. However, the maximum of the Q_F = 15.3 and t_d = 28.1 *fs* can be observed in our proposed hybrid metasurface when h_1 = 90 nm and h_2 = 50 nm. This result will provide the guidance for tuning Fano resonance spectra and the dephasing time t_d in the metal and dielectric hybrid metasurface.

Table 1. Quality factor Q_F and dephasing time t_d versus h_1 and h_2.

	h_1 (nm)				h_2 (nm)			
	30	**50**	**70**	**90**	**30**	**50**	**70**	**90**
Q_F	0.4	4.6	8.5	15.3	14.0	15.3	10.2	12.5
t_d (fs)	10.7	14.0	19.9	28.1	27.3	28.1	23.7	25.0

Generally speaking, the length of each unit in x- and y-directions has great influence on transmission spectra, so we will study the effect of Px and Py on Fano resonances in our proposed hybrid metasurface as shown in Figure 6. Figure 6a–c show transmission spectra as a function of Px when h_1 = 90 nm, h_2 = 50 nm, l = 200 nm, and Py = 400 nm. We can see that the transmission ratio of the left transmission dip obviously decreases, and the transmission spectra show slight red shift as Px increases.

This phenomenon is caused by the coupling between the adjacent structural unit decreases with the increasing of Px. Then, we discuss the transmission spectra as a function of Py when h_1 = 90 nm, h_2 = 50 nm, l = 200 nm, and Px = 400 nm as depicted in Figure 6d–f. We can see that the transmission spectra also show red shift. However, the transmission ratio of the left transmission dip increases when Py increases, which shows the opposite effect compared with Figure 6a–c. This is because that the x-directional polarization of light is chosen in our FDTD simulation. We also calculate the quality factor Q_F and dephasing time t_d of the Fano resonance when the period Px and Py equal to 375 nm, 400 nm, and 425 nm in the proposed hybrid metasurface. We find that the effect of Px and Py on the quality factor Q_F and dephasing time t_d is much less than that for the thickness h_1 and h_2.

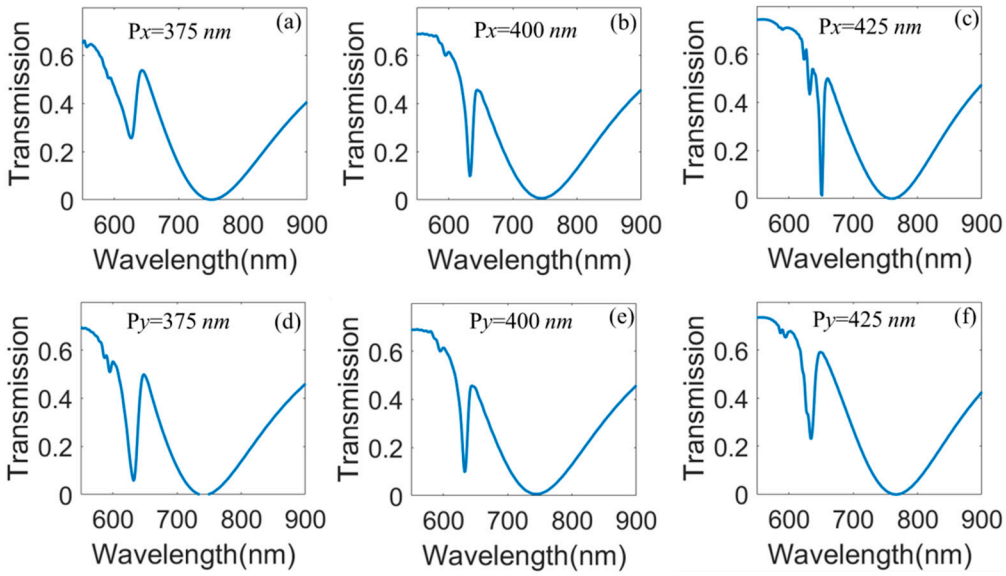

Figure 6. (**a**–**c**) transmission spectra as a function of Px for the proposed hybrid metasurface when h_1 = 90 nm, h_2 = 50 nm, l = 200 nm, and Py = 400 nm; (**d**–**f**) transmission spectra as a function of Py when h_1 = 90 nm, h_2 = 50 nm, l = 200 nm, and Px = 400 nm.

Finally, we investigate the effect of the structural defect on Fano resonances in our proposed hybrid metasurface. Here, we introduce a stub-shaped defect in our proposed structure as shown in Figure 7a, w is the width of the stub, d is the height of the stub, and b is the distance between the stub and the right side of the structure. Figure 7b describes transmission spectra as a function of b when d = 50 nm, w = 50 nm, h_1 = 90 nm, h_2 = 50 nm, l = 200 nm, and Px = Py = 400 nm. The results show that the resonant wavelength of LSPRs increases when b increases from 0 to 75 nm. Furthermore, interesting, single Fano resonance splits into multiple Fano resonances when b increases, which is caused by the present of additional cavity resonance mode besides LSPRs and SPPs in the hybrid metasurface. Then, we study the effect of d on transmission spectra when b = 75 nm, w = 50 nm, h_1 = 90 nm, h_2 = 50 nm, l = 200 nm, and Px = Py = 400 nm as shown in Figure 7b. We can also see that the resonant wavelength of LSPRs increases and obvious double Fano resonances appear when d increases from 25 nm to 75 nm. These results may provide important guidance for regulation of Fano resonances in the Au/TiO_2 hybrid metasurface.

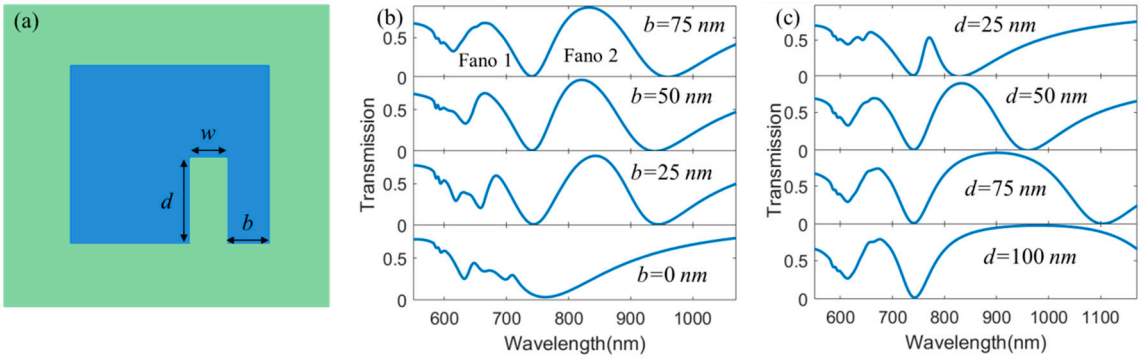

Figure 7. (**a**) *x*–*y* plane view of the schematic diagram for the Au/TiO_2 metasurface with the stub-shaped defect, (**b**) transmission spectra as a function of b when d = 50 nm, w = 50 nm, h_1 = 90 nm, h_2 = 50 nm, l = 200 nm, *and* Px = Py = 400 nm; (**c**) transmission spectra as a function of d when b = 75 nm, w = 50 nm, h_1 = 90 nm, h_2 = 50 nm, l = 200 nm, and Px = Py = 400 nm.

Finally, we also discuss the quality factor Q_F and dephasing time t_d of the Fano resonance in the hybrid metasurface with a stub-shaped defect as shown in Table 2. Fano 1 is the left Fano resonance, and Fano resonance 2 stands for the right Fano resonance in Figure 7b,c. Observing from Table 2, we can see that the quality factors Q_F for the Fano resonance 1 and 2 decrease as the length d increases. Meanwhile, the dephasing time t_d also decreases with the increasing of d. The maximum of dephasing time t_d can reach up to 46.4 *fs* at the Fano resonance 2 when d = 25 nm, b = 75 nm, w = 50 nm, h_1 = 90 nm, h_2 = 50 nm, l = 200 nm, and Px = Py = 400 nm. Moreover, the quality factor Q_F and dephasing time t_d for Fano resonance 1 show obvious increase when b increases. However, the quality factor Q_F and dephasing time t_d for the Fano resonance 2 shows the moderate trend as b increases.

Table 2. Quality factor Q_F and dephasing time t_d versus d and b.

		***d* (nm)**				***b* (nm)**		
		25	50	75	100	25	50	75
Q_F	Fano 1	12.4	9.3	9.3	8.9	9.1	11.1	16.3
	Fano 2	23.4	6.8	3.6	2.4	6.7	7.7	7.7
t_d **(fs)**	Fano 1	32.7	24.4	24.3	23.5	24.0	29.5	38.5
	Fano 2	46.4	21.5	15.0	12.1	20.2	23.1	23.2

3.2. Sensing Enhancement Based on the Stub-Shaped Defect

As is well known, the steep spectra of the Fano resonance can effectively enhance the sensitivity of refractive index sensing. Here, we further study the mechanism of the sensing enhancement by the defect in the proposed hybrid metasurface as shown in Figure 8. We investigate the transmission spectra versus the refractive index of the external environment when h_1 = 90 nm, h_2 = 50 nm, l = 200 nm, and Px = Py = 400 nm in the Au/TiO_2 hybrid metasurface when there are no stub-shaped defects. We can see that the Fano resonance shows a red shift when the refractive index n increases from 1.00 to 1.06. Figure 8c shows the resonant wavelength of the Fano resonance peak versus n; we can find that the resonant wavelength shows a linear increase as the refractive index n increases. The sensitivity is the most important physical parameter to measure sensor characteristics of the structure. Here, we introduce the definition of the sensitivity as $s = \Delta\lambda/\Delta n$, where λ is the resonant wavelength of the Fano resonance. According to this equation, we can calculate the maximum of the sensitivity Max(s)= 90 nm/*RIU* in the proposed hybrid metasurface without the stub-shaped defect. Figure 8e plots the transmission spectra as a function of the refractive index for the external environment when b = 75 nm, d = 50 nm, w = 50 nm, h_1 = 90 nm, h_2 = 50 nm, l = 200 nm, and Px = Py = 400 nm in the Au/TiO_2 hybrid metasurface with the stub-shaped defect. We can see that the transmission spectra

show obvious red shift as the refractive index n increases. The resonant wavelength of the Fano resonance 1 and 2 versus n are depicted in Figure 8f,g. We can see that the resonant wavelengths of the Fano resonance 1 and 2 increase with the increasing of n. In addition, we calculate the maximum of sensitivity at the Fano resonance 1 and 2, and Max(s) = 330 nm/RIU for the Fano resonance 1, Max(s) = 535 nm/RIU for the Fano resonance 2. In particular, the sensitivity in the hybrid metasurface with a stub-shaped defect is three times larger than that in Figure 8c. More importantly, the sensitivity in the proposed Au/TiO_2 hybrid metasurface is much higher than that in the pure TiO_2 metasurface reported in the recent reference [53]. Finally, we investigate the figure of merit (FOM) in our proposed hybrid metasurface as shown in Figure 8d,h. FOM is defined as $(\Delta T/\Delta n)/T$ [58], where $\Delta(T)/\Delta(n)$ is the relative intensity change induced by the refractive index change Δn. Figure 8d shows the FOM of sensing at the fixed wavelength when there is no defect on the proposed Au/TiO_2 hybrid metasurface. We can see that the maximum of FOM can reach up to 60 at the wavelength of 634.1 nm. The FOM for the proposed Au/TiO_2 hybrid metasurface with a stub-shaped defect are shown in Figure 8h. In addition, the maximum of the FOM are equal to 91 at the wavelength of 971 nm when b = 75 nm, d = 50 nm, w = 50 nm, h_1 = 90 nm, h_2 = 50 nm, l = 200 nm, and Px = Py = 400 nm. These results will have great significance for designing ultra-high sensitive nanosensors.

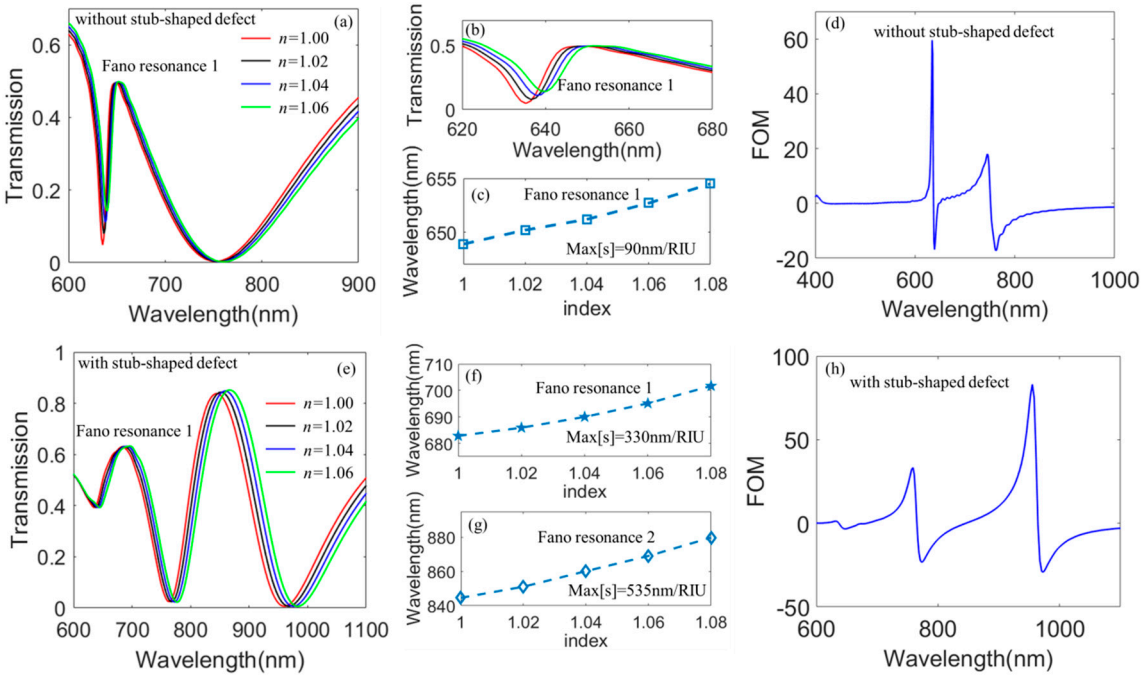

Figure 8. (**a**) transmission spectra as a function of n when h_1 = 90 nm, h_2 = 50 nm, l = 200 nm, and Px = Py = 400 nm in the Au/TiO_2 hybrid metasurface without the stub-shaped defect; (**b**) magnification of the Fano resonance in Figure 8a; (**c**) FOM in the proposed hybrid metasurface without stub-shaped defect; (**d**) resonant wavelength of Fano resonance versus n in Figure 8b; (**e**) transmission spectra as a function of the refractive index for the external environment when b = 75 nm, d = 75 nm, w = 50 nm, h_1 = 90 nm, h_2 = 50 nm, l = 200 nm, and Px = Py = 400 nm in the Au/TiO_2 metasurface with the stub-shaped defect; (**f**) resonant wavelength of the Fano resonance 1 versus n in Figure 8d; (**g**) resonant wavelength of the Fano resonance 2 versus n in Figure 8d; (**h**) FOM in the proposed hybrid metasurface with a stub-shaped defect.

4. Conclusions

In summary, we have studied Fano resonances and its sensing enhancements in the simple Au/TiO_2 metasurface by use of the FDTD simulation method and CMT analysis. We find that the Fano resonance in the proposed hybrid metasurface is caused by the destructive interaction between SPPs

and LSPRs, and the line shape, quality factor Q_F, and dephasing time t_d of the Fano resonance can be effectively tuned by the thickness of the Au layer and TiO_2 layer, the length of each period in the x- and y-directions as well as the structure defect. It is more interesting to note that the stub-shaped defect can make a single Fano resonance spectrum split into multiple Fano resonances, and multiple Fano resonances can be tuned by the size and position of the stub-shaped defect. Moreover, the sensitivity and the FOM in the proposed hybrid metasurface have been studied in detail in our work. We find that the refractive index sensitivity in the Au/TiO_2 hybrid metasurface with the stub-shaped defect can research up to 330 nm/RIU and 535 nm/RIU at the Fano resonance 1 and Fano resonance 2, which is much larger than that in the Au/TiO_2 hybrid metasurface without the stub-shaped defect, and the sensor performance is also obviously better than that in a pure TiO_2 metasurface. We also find that the maximum of the FOM can reach up to 91 at the wavelength of 971 nm when the proposed hybrid metasurface contains the stub-shaped defect. These results may provide a deep understanding of Fano resonances and guidance for designing higher sensitive refractive index sensors.

Author Contributions: Z.H. and W.X. conceived and designed simulation; Z.H., W.C., and C.L. performed the simulation; Z.H., Z.L., L.P., and G.L. analyzed the data; J.F., X.X., and X.W. contributed reagents/materials/analysis tools; Z.H. wrote and revised the paper. All authors have read and agreed to the published version of the manuscript.

Funding: This work was supported by the National Natural Science Foundation of China (NSFC) (11847026 and 11947100); the China Postdoctoral Science Foundation Funded Project (2019M653722); the Natural Science Basic Research Plan in Shaanxi Province of China (2019JQ-357 and 2018JQ1056); Young People's Referral Program of Shaanxi Science and Technology Association (20170113); the Education Department Program of Shaanxi (19JK0971); and the Youth Project of Research Program Yan'an University (YDY2019-20, YDQ2019-17, and YDBK2017-29).

Conflicts of Interest: The authors declare no conflicts of interest.

References

1. Pendry, J.B.; Martin-Moreno, L.; Garcia-Vidal, F.J. Mimicking surface plasmons with structured surfaces. *Science* **2004**, *305*, 847–848. [CrossRef] [PubMed]
2. Hibbins, A.P.; Evans, B.R.; Sambles, J.R. Experimental verification of designer surface plasmons. *Science* **2005**, *308*, 670–672. [CrossRef] [PubMed]
3. Chang, D.E.; Sørensen, A.S.; Demler, E.A.; Lukin, M.D. A single-photon transistor using nanoscale surface plasmons. *Nat. Phys.* **2007**, *3*, 807–812. [CrossRef]
4. Chong, M.C.; Reecht, G.; Bulou, H.; Boeglin, A.; Scheurer, F.; Mathevet, F.; Schull, G. Narrow-line single-molecule transducer between electronic circuits and surface plasmons. *Phys. Rev. Lett.* **2016**, *116*, 036802. [CrossRef] [PubMed]
5. Lereu, A.L.; Zerrad, M.; Passian, A.; Amra, C. Surface plasmons and Bloch surface waves: Towards optimized ultra-sensitive optical sensors. *Appl. Phys. Lett.* **2017**, *111*, 011107. [CrossRef]
6. He, Z.; Li, H.; Li, B.; Chen, Z.; Xu, H.; Zheng, M. Theoretical analysis of ultrahigh figure of merit sensing in plasmonic waveguides with a multimode stub. *Opt. Lett.* **2016**, *41*, 5206–5209. [CrossRef] [PubMed]
7. Zhan, S.; Li, H.; He, Z.; Li, B.; Chen, Z.; Xu, H. Sensing analysis based on plasmon induced transparency in nanocavity-coupled waveguide. *Opt. Express* **2015**, *23*, 20313–20320. [CrossRef]
8. Fedeli, L.; Sgattoni, A.; Cantono, G.; Garzella, D.; Réau, F.; Prencipe, I.; Macchi, A. Electron acceleration by relativistic surface plasmons in laser-grating interaction. *Phys. Rev. Lett.* **2016**, *116*, 015001. [CrossRef]
9. Zhan, S.; Xiong, J.; Nie, G.; Wu, S.; Hu, J.; Wu, X.; Liu, Y. Steady State Luminescence Enhancement in Plasmon Coupled Core/Shell Upconversion Nanoparticles. *Adv. Mater. Interfaces* **2019**, *6*, 1802089. [CrossRef]
10. Guzzinati, G.; Béché, A.; Lourenco-Martins, H.; Martin, J.; Kociak, M.; Verbeeck, J. Probing the symmetry of the potential of localized surface plasmon resonances with phase-shaped electron beams. *Nat. Commun.* **2017**, *8*, 14999. [CrossRef]
11. Gao, E.; Liu, Z.; Li, H.; Xu, H.; Zhang, Z.; Luo, X.; Zhou, F. Dynamically tunable dual plasmon-induced transparency and absorption based on a single-layer patterned graphene metamaterial. *Opt. Express* **2019**, *27*, 13884–13894. [CrossRef] [PubMed]
12. Xu, H.; Li, H.; He, Z.; Chen, Z.; Zheng, M.; Zhao, M. Theoretical analysis of optical properties and sensing in a dual-layer asymmetric metamaterial. *Opt. Commun.* **2018**, *407*, 250–254. [CrossRef]

13. Murray, W.A.; Suckling, J.R.; Barnes, W.L. Overlayers on silver nanotriangles: Field confinement and spectral position of localized surface plasmon resonances. *Nano Lett.* **2006**, *6*, 1772–1777. [CrossRef] [PubMed]
14. Qin, F.; Chen, Z.; Chen, X.; Yi, Z.; Yao, W.; Duan, T.; Yi, Y. A Tunable Triple-Band Near-Infrared Metamaterial Absorber Based on Au Nano-Cuboids Array. *Nanomaterials* **2020**, *10*, 207. [CrossRef] [PubMed]
15. He, Z.; Li, H.; Zhan, S.; Cao, G.; Li, B. Combined theoretical analysis for plasmon-induced transparency in waveguide systems. *Opt. Lett.* **2014**, *39*, 5543–5546. [CrossRef] [PubMed]
16. Zhan, S.; Li, H.; Cao, G.; He, Z.; Li, B.; Yang, H. Slow light based on plasmon-induced transparency in dual-ring resonator-coupled MDM waveguide system. *J. Phys. D Appl. Phys.* **2014**, *47*, 205101. [CrossRef]
17. Wang, Y.; Qin, F.; Yi, Z.; Chen, X.; Zhou, Z.; Yang, H.; Yi, Y. Effect of slit width on surface plasmon resonance. *Results Phys.* **2019**, *15*, 102711. [CrossRef]
18. He, Z.; Zhao, J.; Lu, H. Tunable nonreciprocal reflection and its stability in a non-PT-symmetric plasmonic resonators coupled waveguide systems. *Appl. Phys. Express* **2020**, *13*, 012009. [CrossRef]
19. He, Z.; Peng, Y.; Li, B.; Chen, Z.; Xu, H.; Zheng, M.; Li, H. Aspect ratio control and sensing applications for a slot waveguide with a multimode stub. *Appl. Phys. Express* **2016**, *9*, 072002. [CrossRef]
20. Shafiei, F.; Monticone, F.; Le, K.Q.; Liu, X.X.; Hartsfield, T.; Alù, A.; Li, X. A subwavelength plasmonic metamolecule exhibiting magnetic-based optical Fano resonance. *Nat. Nanotechnol.* **2013**, *8*, 95. [CrossRef]
21. Rahmani, M.; Luk'yanchuk, B.; Hong, M. Fano resonance in novel plasmonic nanostructures. *Laser Photonics Rev.* **2013**, *7*, 329–349. [CrossRef]
22. Cao, G.; Li, H.; Deng, Y.; Zhan, S.; He, Z.; Li, B. Plasmon-induced transparency in a single multimode stub resonator. *Opt. Express* **2014**, *22*, 25215–25223. [CrossRef] [PubMed]
23. Xu, H.; Li, H.; He, Z.; Chen, Z.; Zheng, M.; Zhao, M. Dual tunable plasmon-induced transparency based on silicon–air grating coupled graphene structure in terahertz metamaterial. *Opt. Express* **2017**, *25*, 20780–20790. [CrossRef] [PubMed]
24. Zhang, B.; Li, H.; Xu, H.; Zhao, M.; Xiong, C.; Liu, C.; Wu, K. Absorption and slow-light analysis based on tunable plasmon-induced transparency in patterned graphene metamaterial. *Opt. Express* **2019**, *27*, 3598–3608. [CrossRef] [PubMed]
25. Wang, Y.; Chen, Z.; Xu, D.; Yi, Z.; Chen, X.; Chen, J.; Yi, Y. Triple-band perfect metamaterial absorber with good operating angle polarization tolerance based on split ring arrays. *Results Phys.* **2020**, *16*, 102951. [CrossRef]
26. Chen, Z.; Li, H.; Zhan, S.; He, Z.; Li, B.; Xu, H. Sensing characteristics based on Fano resonance in rectangular ring waveguide. *Opt. Commun.* **2015**, *356*, 373–377. [CrossRef]
27. Zhang, S.; Genov, D.A.; Wang, Y.; Liu, M.; Zhang, X. Plasmon-induced transparency in metamaterials. *Phys. Rev. Lett.* **2008**, *101*, 047401. [CrossRef]
28. Kekatpure, R.D.; Barnard, E.S.; Cai, W.; Brongersma, M. Phase-coupled plasmon-induced transparency. *Phys. Rev. Lett.* **2010**, *104*, 243902. [CrossRef]
29. Liu, C.; Li, H.; Xu, H.; Zhao, M.; Xiong, C.; Zhang, B.; Wu, K. Tunable plasmon-induced transparency absorbers based on few-layer black phosphorus ribbon metamaterials. *J. Opt. Soc. Am. B* **2019**, *36*, 3060–3065. [CrossRef]
30. Liu, C.; Li, H.; Xu, H.; Zhao, M.; Xiong, C.; Zhang, B.; Wu, K. Slow light effect based on tunable plasmon-induced transparency of monolayer black phosphorus. *J. Phys. D Appl. Phys.* **2019**, *52*, 405203. [CrossRef]
31. Ma, R.M.; Oulton, R.F.; Sorger, V.J.; Bartal, G.; Zhang, X. Room-temperature sub-diffraction-limited plasmon laser by total internal reflection. *Nat. Mater.* **2011**, *10*, 110–113. [CrossRef] [PubMed]
32. Pu, M.B.; Wang, C.T.; Wang, Y.Q.; Luo, X.G. Subwavelength electromagnetics below the diffraction limit. *Acta Phys. Sin.* **2017**, *66*, 144101.
33. Ebbesen, T.W.; Lezec, H.J.; Ghaemi, H.F.; Thio, T.; Wolff, P.A. Extraordinary optical transmission through sub-wavelength hole arrays. *Nature* **1998**, *391*, 667–669. [CrossRef]
34. Martin-Moreno, L.; Garcia-Vidal, F.J.; Lezec, H.J.; Pellerin, K.M.; Thio, T.; Pendry, J.B.; Ebbesen, T.W. Theory of extraordinary optical transmission through subwavelength hole arrays. *Phys. Rev. Lett.* **2001**, *86*, 1114. [CrossRef]
35. Chen, Z.; Li, P.; Zhang, S.; Chen, Y.; Liu, P.; Duan, H. Enhanced extraordinary optical transmission and refractive-index sensing sensitivity in tapered plasmonic nanohole arrays. *Nanotechnology* **2019**, *30*, 335201. [CrossRef]
36. Safavi-Naeini, A.H.; Alegre, T.P.M.; Chan, J.; Eichenfield, M.; Winger, M.; Lin, Q.; Painter, O. Electromagnetically induced transparency and slow light with optomechanics. *Nature* **2011**, *472*, 69–73. [CrossRef]

37. Gu, J.; Singh, R.; Liu, X.; Zhang, X.; Ma, Y.; Zhang, S.; Taylor, A.J. Active control of electromagnetically induced transparency analogue in terahertz metamaterials. *Nat. Commun.* **2012**, *3*, 1151. [CrossRef]
38. Liu, N.; Langguth, L.; Weiss, T.; Kästel, J.; Fleischhauer, M.; Pfau, T.; Giessen, H. Plasmonic analogue of electromagnetically induced transparency at the Drude damping limit. *Nat. Mater.* **2009**, *8*, 758–762. [CrossRef]
39. Cao, G.; Li, H.; Zhan, S.; Xu, H.; Liu, Z.; He, Z.; Wang, Y. Formation and evolution mechanisms of plasmon-induced transparency in MDM waveguide with two stub resonators. *Opt. Express* **2013**, *21*, 9198–9205. [CrossRef]
40. Cao, G.; Li, H.; Zhan, S.; He, Z.; Guo, Z.; Xu, X.; Yang, H. Uniform theoretical description of plasmon-induced transparency in plasmonic stub waveguide. *Opt. Lett.* **2014**, *39*, 216–219. [CrossRef]
41. Zhan, S.; Li, H.; Cao, G.; He, Z.; Li, B.; Xu, H. Theoretical analysis and applications on nano-block loaded rectangular ring. *J. Opt. Soc. Am. A* **2014**, *31*, 2263–2267. [CrossRef] [PubMed]
42. Xu, H.; Zhao, M.; Zheng, M.; Xiong, C.; Zhang, B.; Peng, Y.; Li, H. Dual plasmon-induced transparency and slow light effect in monolayer graphene structure with rectangular defects. *J. Phys. D Appl. Phys.* **2018**, *52*, 025104. [CrossRef]
43. Liu, N.; Weiss, T.; Mesch, M.; Langguth, L.; Eigenthaler, U.; Hirscher, M.; Giessen, H. Planar metamaterial analogue of electromagnetically induced transparency for plasmonic sensing. *Nano Lett.* **2010**, *10*, 1103–1107. [CrossRef] [PubMed]
44. Eftekhari, F.; Escobedo, C.; Ferreira, J.; Duan, X.; Girotto, E.M.; Brolo, A.G.; Sinton, D. Nanoholes as nanochannels: Flow-through plasmonic sensing. *Anal. Chem.* **2009**, *81*, 4308–4311. [CrossRef]
45. Rindzevicius, T.; Alaverdyan, Y.; Dahlin, A.; Höök, F.; Sutherland, D.S.; Käll, M. Plasmonic sensing characteristics of single nanometric holes. *Nano Lett.* **2005**, *5*, 2335–2339. [CrossRef]
46. Luk'yanchuk, B.; Zheludev, N.I.; Maier, S.A.; Halas, N.J.; Nordlander, P.; Giessen, H.; Chong, C.T. The Fano resonance in plasmonic nanostructures and metamaterials. *Nat. Mater.* **2010**, *9*, 707–715. [CrossRef]
47. Singh, R.; Cao, W.; Al-Naib, I.; Cong, L.; Withayachumnankul, W.; Zhang, W. Ultrasensitive terahertz sensing with high-Q Fano resonances in metasurfaces. *Appl. Phys. Lett.* **2014**, *105*, 171101. [CrossRef]
48. Abujetas, D.R.; Sáenz, J.J.; Sánchez-Gil, J.A. Narrow Fano resonances in Si nanocylinder metasurfaces: Refractive index sensing. *J. Appl. Phys.* **2019**, *125*, 183103. [CrossRef]
49. Gerislioglu, B.; Dong, L.; Ahmadivand, A.; Hu, H.; Nordlander, P.; Halas, N.J. Monolithic metal dimer-on-film structure: New plasmonic properties introduced by the underlying metal. *Nano Lett.* **2020**, *20*, 2087–2093. [CrossRef]
50. Lu, H.; Liu, X.; Mao, D.; Wang, G. Plasmonic nanosensor based on Fano resonance in waveguide-coupled resonators. *Opt. Lett.* **2012**, *37*, 3780–3782. [CrossRef]
51. Zhan, S.; Peng, Y.; He, Z.; Li, B.; Chen, Z.; Xu, H.; Li, H. Tunable nanoplasmonic sensor based on the asymmetric degree of Fano resonance in MDM waveguide. *Sci. Rep.* **2016**, *6*, 22428. [CrossRef] [PubMed]
52. Tang, W.; Wang, L.; Chen, X.; Liu, C.; Yu, A.; Lu, W. Dynamic metamaterial based on the graphene split ring high-Q Fano-resonnator for sensing applications. *Nanoscale* **2016**, *8*, 15196–15204. [CrossRef] [PubMed]
53. Zhang, Y.; Li, T.; Zeng, B.; Zhang, H.; Lv, H.; Huang, X.; Azad, A.K. A graphene based tunable terahertz sensor with double Fano resonances. *Nanoscale* **2015**, *7*, 12682–12688. [CrossRef] [PubMed]
54. Cen, C.; Chen, Z.; Xu, D.; Jiang, L.; Chen, X.; Yi, Z.; Yi, Y. High Quality Factor, High Sensitivity Metamaterial Graphene—Perfect Absorber Based on Critical Coupling Theory and Impedance Matching. *Nanomaterials* **2020**, *10*, 95. [CrossRef] [PubMed]
55. Liu, H.; Zheng, L.; Ma, P.; Zhong, Y.; Liu, B.; Chen, X.; Liu, H. Metasurface generated polarization insensitive Fano resonance for high-performance refractive index sensing. *Opt. Express* **2019**, *27*, 13252–13262. [CrossRef]
56. Klar, T.; Perner, M.; Grosse, S.; Von Plessen, G.; Spirkl, W.; Feldmann, J. Surface-plasmon resonances in single metallic nanoparticles. *Phys. Rev. Lett.* **1998**, *80*, 4249. [CrossRef]
57. Ahmadivand, A.; Gerislioglu, B.; Ramezani, Z. Gated graphene island-enabled tunable charge transfer plasmon terahertz metamodulator. *Nanoscale* **2019**, *11*, 8091–8095. [CrossRef]
58. Liu, N.; Mesch, M.; Weiss, T.; Hentschel, M.; Giessen, H. Infrared perfect absorber and its application as plasmonic sensor. *Nano Lett.* **2010**, *10*, 2342–2348. [CrossRef]